Research Article Vol. 63, No. 30 / 30 October 2024 / Applied Optics 7893

applied optics

Spatial resolution limit for a solid immersion lens

Vladislav A. Zhelnov,[1] Vladislav E. Ulitko,[2] Maksim Skorobogatiy,[2] Kirill I. Zaytsev,[1,3] and Nikita V. Chernomyrdin[1,*]

[1]Prokhorov General Physics Institute of the Russian Academy of Sciences, 119991 Moscow, Russia
[2]Department of Engineering Physics, Polytechnique Montréal, Montreal, Quebec H3C 3A7, Canada
[3]kirzay@gmail.com
*chernik-a@yandex.ru

Received 17 July 2024; revised 17 September 2024; accepted 25 September 2024; posted 26 September 2024; published 14 October 2024

The solid immersion (SI) effect is widely used to increase the spatial resolution of optical focusing systems and even overcome the Abbe diffraction limit. Resolution enhancement offered by a SI lens is mostly a function of its geometry and refractive index n_{SI}. While SI lenses are relatively well understood, the scaling of the resolution enhancement by such lenses is still a subject of debate, with some works reporting $\simeq n_{\mathrm{SI}}$ and $\simeq n_{\mathrm{SI}}^2$ dependencies for the hemispherical and hyperhemispherical SI lens configurations, respectively. In this paper, we offer a general argument for a resolution limit for SI optics and, then, verify it via the numerical analysis of the hemispherical and hyperhemispherical silicon SI lenses designed for the terahertz (THz) range. In fact, we find that there is no contradiction in the reported resolution enhancements $\simeq n_{\mathrm{SI}}$ and $\simeq n_{\mathrm{SI}}^2$; however, they happen in different operation regimes. We then demonstrate that the resolution values reported for the different SI lens arrangements in the visible (VIS), near-, and middle-infrared (NIR and MIR), as well as THz bands obey the derived limit. Our findings will be useful for the further design and applications of SI optics.

https://doi.org/10.1364/AO.536928

1. INTRODUCTION

Since the discovery of the SI effect in 1990 by Mansfield and Kino [1], it has been vigorously explored and applied in a variety of optical systems, operating in different spectral ranges. The SI effect makes it possible to improve the spatial resolution of almost any focusing system and even overcome the $\simeq 0.5\lambda$ Abbe diffraction limit of free-space focusing (λ is a wavelength of light in free space), while sustaining high energy efficiency thanks to the absence of any sub-wavelength apertures or probes in the optical assembly [2,3]. The essence of the SI effect is a reduction in the dimensions of the beam focal spot, when it is focused at a small distance ($<\lambda$) behind a back surface of a high-refractive-index (n_{SI}) SI lens. Both propagating waves (undergoing the ordinary reflection/transmission at the back surface of a SI lens) and evanescent waves [excited due to the total internal reflection (TIR) and propagating along the surface] contribute to such a focusing (Fig. 1). The resolution enhancement offered by a SI lens increases with the lens refractive index n_{SI} in a different manner for the distinct SI lens arrangements. Another complication is that the resolution depends on the complex refractive index of an imaged object [4].

Thanks to the conceptual simplicity, impressive resolution, and high energy efficiency, SI optics found numerous applications in different branches of science and technology [2,3], including the super-resolution microscopy in the VIS [5], NIR, and MIR [6] ranges, Raman [7] and photoluminescence [8] microscopy, condensed matter physics and superconductivity [2,6,9], quantum science [10], data storage [11], non-destructive testing [12], and biomedicine [13]. Recently, the SI effect was used in the THz range [14,15] (frequencies of 0.1–10 THz, wavelengths of 3 mm–30 μm).

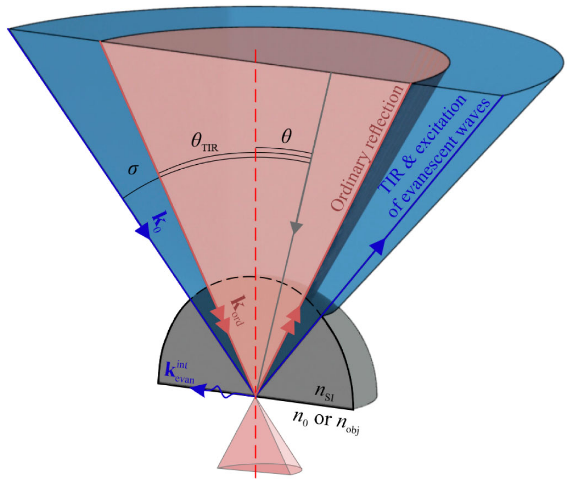

Fig. 1. Schematic of the spherical wave focusing at the shadow side of a hemispherical SI lens, where a first focusing element (a standard wide-aperture lens) is not shown, for simplicity.

Our group developed the reflection-mode continuous-wave 0.15λ-resolution THz SI microscope [16] based on a wide-aperture aspherical polymer singlet [17] and a hemispherical SI lens made of the high-resistivity float-zone silicon (HRFZ-Si, $n_{Si} \simeq 3.414$). We use a composite SI hemisphere, comprising the rigidly fixed hypohemisphere and a movable flat window, which form a unitary optical element. The window serves as a sample holder and moves together with a sample to raster scan its surface by a focused beam, which makes possible the THz imaging of soft tissues [16,18,19]. We also developed the quantitative (capable of retrieving the local THz dielectric response of an analyte) [18], polarization-sensitive [19], and endoscopic [20] modalities of the THz SI microscopy by using the different THz optical materials and SI lens arrangements. The THz SI microscopy was adapted to work with the broadband THz photoconductive antennas [21,22]. The most advanced THz SI lens based on rutile (monocrystalline TiO_2, $n_{TiO_2} \sim 10$) demonstrated the resolution record of $0.06 - 0.11\lambda$ [23].

Despite a strong interest in SI optics, there is still no consensus on the maximal achievable resolution in such systems [2,3]. In fact, the standard methods employed for optical systems' design and optimization rely on the principles of geometrical optics, scalar diffraction theory, and Fourier optics. Such methods fail to provide reasonable predictions for the resolution of a SI lens, due to its wide aperture, near-field operation, and important contribution of evanescence waves. Therefore, the resolution of SI lenses can be reliably analyzed by employing the full-vectorial full-wave numerical analysis or experiments [4,8,16,18,23–27]. Such analysis is still largely lacking in the literature. In this paper, we offer a general argument for a resolution limit for SI optics and verify it by a full-wave numerical analysis of the THz-wave focusing by the common hemispherical and hyperhemispherical reflection-mode SI lenses made of the HRFZ-Si. We then demonstrate that the earlier-reported resolution estimates for the VIS, NIR, MIR, and THz SI lenses also respect the derived limit. Additionally, relying on the numerical data, we compare the energy efficiency of the hemispherical and hyperhemispherical SI lenses.

2. RESOLUTION LIMIT FOR A SI LENS

In Fig. 1, a schematic of the electromagnetic-beam focusing by a hemispherical SI lens is presented. Depending on the incidence angle of the incoming light, two light propagation regimes are possible [3]. At small incidence angles, the light will traverse the lens/object interface by undergoing the ordinary Fresnel reflection/transmission [incidence angles smaller than the critical TIR one $\theta < \theta_{TIR} = \arcsin(n_{obj}/n_{SI})$, where n_{obj} is the refractive index of an object]. At higher incidence angles $\theta_{TIR} \leq \theta \leq \sigma$, TIR at the lens/object boundary takes place leading to the excitation of the evanescent waves. The beam caustic is formed as a result of constructive interference of the propagating and evanescent waves in the close proximity to the SI lens back surface [3].

The resolution enhancement for the reflection-mode SI lens resulted from the electromagnetic wavelength reduction near the analyzed interface (as compared to a free-space wavelength λ) both for ordinary-reflected and evanescent waves. The ordinary wave propagates through the high-refractive-index SI lens material and is characterized by the following wavevector $\mathbf{k}_{ord}$ and wavelength λ_{ord}:

$$\mathbf{k}_{ord} = \mathbf{k}_0 n_{SI}, \quad \lambda_{ord} = \frac{\lambda}{n_{SI}}, \tag{1}$$

where $\mathbf{k}_0$ is a free-space wavevector. Here, λ_{ord} is n_{SI}-times smaller than λ. The evanescent wave is excited at the SI lens–object interface and propagates along this interface with the wavevector $\mathbf{k}_{evan}^{int}$ and the effective wavelength λ_{evan} of

$$\mathbf{k}_{evan}^{int} = \mathbf{k}_0 n_{SI} \sin\theta, \quad \lambda_{evan} = \frac{\lambda}{n_{SI}\sin\theta}. \tag{2}$$

Here λ_{evan} is also reduced by a factor of $n_{SI}\sin\theta$ (or even $\sim n_{SI}$ at high apertures θ) as compared to λ. The interference of these waves leads to the intensity patterns along the interface with the minimal dimensions of $\delta_{SI} \equiv \lambda_{ord}/2 \simeq \lambda_{evan}/2$. Thus, the resolution limit for a SI lens can be defined as

$$\delta_{SI} = \frac{\lambda}{2n_{SI}}. \tag{3}$$

It appears to be a function of only the SI lens refractive index n_{SI} and the free-space wavelength λ. Owing to the wave nature of light, SI lenses of any configuration cannot overcome this limitation, including the much studied hemispherical and hyperhemispherical SI lenses [2]. It is worth noting that despite the contribution of evanescent waves to the electromagnetic-wave focusing by a SI lens, the derived resolution limit appears to be quite similar to the Abbe diffraction limit for the focusing inside a bulk solid material, or an immersion liquid. Remarkably, the resolution limit given by Eq. (3) has not been reported for a SI optics yet.

We should note that the proposed resolution limit Eq. (3) is derived and can be applied only for the optical systems based on the SI effect. Meanwhile it is not suitable for other near-field imaging techniques, such as the dielectric-microparticle-assisted and scanning-probe near-field optical microscopy.

3. NUMERICAL ANALYSIS OF THE HEMISPHERICAL AND HYPERHEMISPHERICAL SI LENSES

To verify this prediction, we numerically analyze the two most-common SI lens geometries. They are comprised of an identical basic focusing element (a standard wide-aperture lens that forms a convergent wavefront with an aperture angle σ) and different HRFZ-Si SI lenses with $n_{SI} = 3.414$, negligible dispersion, and loss in the THz range [16]. We study the SI lenses of two types–namely, the hemispherical and hyperhemispherical SI lenses [Figs. 2(a) and 2(b)] with the beam focusing in the different aplanatic points of a sphere [2].

- The hemispherical SI lens [Fig. 2(a)] with the radius $R = 5$ mm uses the first aplanatic point coinciding with the center of the sphere, or the center of its planar cut. The incident convergent spherical wavefront is concentric to the SI lens spherical surface (no refraction occurs at this surface). Such a SI lens commonly offers the resolution enhancement of $\approx n_{SI}$.
- The hyperhemispherical SI lens, also known as the Weierstrass or super-SI lens [Fig. 2(b)], has the same radius

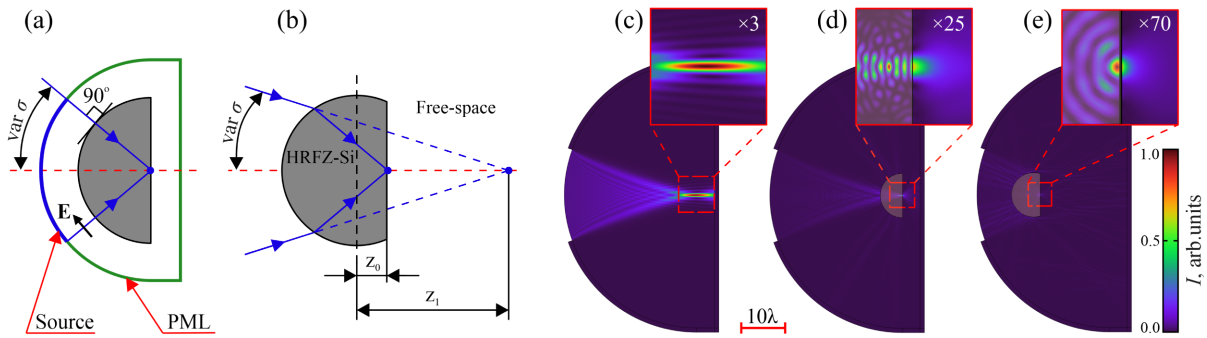

Fig. 2. Numerical 2D FEFD modeling of SI lenses. (a), (b) Schematics of the hemispherical and hyperhemispherical HRFZ-Si SI lenses, along with the numerical modeling domains. The blue arch is a source of a linearly polarized spherical wave with an adjustable aperture angle σ. The green curve shows the PML boundary. The scattered light is TE polarized. (c)–(e) Field intensity distributions $I \propto |\mathbf{E}|^2$ for the focused spherical wave ($\sigma = 40^\circ$, $\lambda = 500$ µm) in free space, or behind the hemispherical and hyperhemispherical lenses, respectively. Inserts show close-ups of the beam caustics.

$R = 5$ mm and exploits the second aplanatic point spaced at the distance $z_0 = R n_0 / n_{\mathrm{SI}}$ from the center of the sphere, where $n_0 = 1$ is the free-space refractive index. The lens thickness $R + z_0 = 6.46$ mm ensures the beam focusing at the planar cut of the sphere, while the center of the sphere is located in front of the focal point of the basic focusing element, at the distance of $z_1 = R n_{\mathrm{SI}} / n_0 = 17.1$ mm. For such a SI lens, the resolution enhancement is predicted to be as high as $\approx n_{\mathrm{SI}}^2$. The superlinear scaling of the resolution enhancement is attributed to the additional refraction at the spherical surface and suggests that, for SI lenses of sufficiently high refractive index, the hyperhemispherical geometry should offer better resolution than the hemispherical one. It also violates the theoretical limit stated in Eq. (3).

The described hemispherical SI lens is equal to that detailed in our previous research [16,18]. In Figs. 2(a) and 2(b), both lenses are illuminated from the left by a convergent spherical monochromatic wave with an adjustable aperture angle σ and the frequency of $\nu \simeq 0.6$ THz (the wavelength of $\lambda = 500$ µm). The radii R and refractive index n_{SI} of these lenses make them large at the scale posed by the wavelength $\lambda \ll 2 R n_{\mathrm{SI}}$.

The finite-element frequency-domain (FEFD) method within the COMSOL MultiPhysics software is applied to numerically analyze the two SI lenses. In order to reduce the simulation time and complexity, we employ the 2D geometry (cylindrical optical elements), assuming that characteristics of the 2D and 3D optical systems do not differ qualitatively [4]. The full-wave 2D simulations take into account all the main features of the electromagnetic-wave–lens interaction and should provide correct scaling relations for SI optics [4,18]. In Figs. 2(a) and 2(b), a scheme of our numerical analysis is shown, where the basic focusing element is substituted by a source of a convergent spherical wave with a finite aperture σ. Such a source helps to directly compare the performance of the two SI lenses, while avoiding any issues on aberrations, Fresnel-loss, and apodization of the beam in a basic focusing element. In this way, the lenses are illuminated with a spherical wave of homogeneous intensity distribution over the aperture and transverse electric (TE) polarization (i.e., the electric field vector $\mathbf{E}$ is in the drawing plane). The perfectly matched layers (PMLs) are positioned at the computational cell extremities to absorb scattered waves. Meshing with the deeply subwavelength maximal element size $\ll \lambda / n_{\mathrm{SI}}$ is used.

In Figs. 2(c)–2(e), the beam intensity distributions $I(\mathbf{r}) \propto |\mathbf{E}(\mathbf{r})|^2$ are calculated for the empty space and the two SI lenses with $\sigma = 40^\circ$. The spatial resolution values δ were estimated from thus calculated beam spots at the full-width at half-maximum (FWHM) level and, then, normalized to the wavelength λ. For the SI lenses, the beam spot geometry is analyzed in free space, at a short distance (≈ 1 µm) behind their flat surfaces. In Fig. 3(a), we compare the calculated normalized resolution parameter δ/λ as a function of the aperture angle σ for the beam focusing in free space, and behind the hemispherical and hyperhemispherical SI lenses. For convenience, we also indicate the free-space $\simeq 0.5\lambda$ Abbe limit and the derived SI lens resolution limit of $\delta_{\mathrm{SI}} \simeq 0.146\lambda$, calculated for the particular wavelength and the HRFZ-Si material. Interestingly, the beam spot observed in the case of free-space focusing becomes slightly smaller than the $\simeq 0.5\lambda$ Abbe limit at high aperture angles $\sigma > 60^\circ$, which was reported in the literature as the resolution limit being affected by the particular intensity distribution over the beam aperture [28,29]. In Fig. 3(b), the resolution enhancement is shown by dividing the size of a focused beam in free space by that formed by the SI lenses.

From Figs. 3(a) and 3(b), we notice that both SI lenses overcome the free-space $\simeq 0.5\lambda$ Abbe resolution limit. The hemispherical SI lens provides a moderate resolution enhancement, which is close to the expected value $n_{\mathrm{SI}} = 3.42$ and monotonically decreases with increasing aperture angle σ. At higher angles $\sigma > 60^\circ$, the SI hemisphere resolution reaches the derived resolution limit δ_{SI} [Eq. (3)]. In turn, the hyperhemispherical SI lens provides the overall higher resolution enhancement. At lower apertures $\sigma < 20^\circ$, it is close to the expected value $n_{\mathrm{SI}}^2 = 11.7$. While increasing the aperture angle σ, the resolution enhancement decreases monotonically. At higher aperture angles $\sigma > 60^\circ$, the resolution enhancement of the SI hyperhemisphere becomes close to that of the SI hemisphere and approaches the inferred limit δ_{SI} [Eq. (3)]. From this, we conclude that the superlinear resolution enhancement $\simeq n_{\mathrm{SI}}^2$, well-known for the SI hyperhemisphere from the literature [2], is only achieved at low aperture values, where the resultant spatial resolution of the total optical system is well above the fundamental limit δ_{SI}. When increasing the aperture angle, both

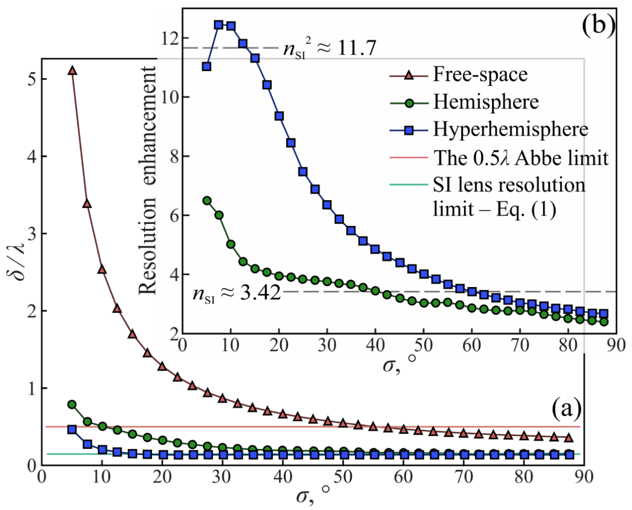

Fig. 3. Numerical 2D FEFD estimates for the spatial resolution of the free-space and SI focusing systems. (a) Normalized resolution parameter δ/λ, as a function of the aperture angle σ, for the free-space focusing, and the hemispherical and hyperhemispherical HRFZ-Si SI lenses, as compared to the $\simeq 0.5\lambda$ Abbe limit and the derived resolution limit for a SI lens [Eq. (3)]. (b) Resolution enhancement factor for the two SI lenses, with the theoretical predictions of $\simeq n_{SI}$ and $\simeq n_{SI}^2$ shown in gray.

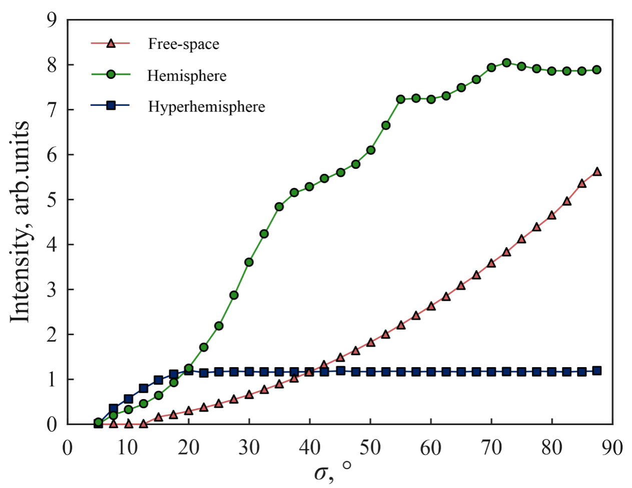

Fig. 4. Numerical 2D FEFD simulations of the focal-spot intensity for the free-space focusing, and hemispherical and hyperhemispherical SI lenses, as a function of the aperture angle σ.

hemispherical and hyperhemispherical SI lenses reach the same fundamental resolution limit given by δ_{SI} [Eq. (3)] resulting in the same resolution enhancement of $\simeq n_{SI}$.

As mentioned above, along with the superior resolution, high energy efficiency forms a main advantage of SI microscopy. Relying on our 2D FEFD data, we also analyzed the focal-spot intensity for the free-space focusing, as well as at the shadow side of the hemispherical and hyperhemispherical THz SI lenses made of the HRFZ-Si material. In Fig. 4, for the considered focusing systems, we show the maximal intensity of the focal spot, as a function of the aperture angle σ. We notice that the hyperhemispherical SI lens provides the highest intensity at lower apertures $\sigma \leq 20°$. In turn, at higher angles $\sigma > 20°$, the hemispherical SI lens offers the higher energy efficiency. When the aperture angle further increases $\sigma > 40°$, the energy efficiency of the hyperhemispherical SI lens appears to be even lower than that of the hemispherical one and the free-space focusing. In this way, when the energy efficiency of an optical system is critical, the hyperhemisphere should be applied at lower apertures $\sigma \leq 20°$, while the hemisphere–at higher ones $\sigma > 20°$. The observed interplay between the lens geometry, aperture angle, and focal-spot intensity can be attributed to the angular-dependent Fresnel reflections at the interfaces. In what follows, such an analysis is relevant only for the considered HRFZ-Si material at THz frequencies, and it should be repeated when resorting to other geometry, material, or operation wavelength of a SI lens.

4. RESOLUTION OF THE EARLIER-REPORTED SI LENSES

Next, we analyze the literature data on the spatial resolution of the different SI lens arrangements. We consider only those works where the resolution is characterized using standard criteria (such as the Rayleigh size, or the FWHM of the central maximum in the beam spot), or measured experimentally involving common approaches (such as the direct beam spot visualization, or imaging using a razor blade) [23]. The SI systems characterized by any non-common resolution criterion, or boosted by some image reconstruction procedures (for example, see Ref. [13]) are excluded from our analysis. In Fig. 5, we show the resolution limit normalized by the operation wavelength δ_{SI}/λ as a function of the SI lens refractive index n_{SI} [Eq. (3)]. We use the literature for the VIS, NIR, MIR, and THz SI lenses fabricated of different high-refractive-index optical materials, such as glasses [1,11,24,30,31], sapphire (monocrystalline $\alpha-Al_2O_3$) [9,14], zirconium dioxide (ZrO_2) [32], silicon (Si, including HRFZ-Si) [6,15,16,22,33–38], pressed titanium dioxide micropowder and a compound of titanium dioxide and polypropylene microparticles (TiO_2/PP) [21], as well as bulk rutile (monocrystalline TiO_2) with its impressive THz refractive index (~10) and the highest resolution values ever reported for the SI optics ($0.06 - 0.11\lambda$) [23]. We notice that, while most of these SI lenses overcome the free-space $\simeq 0.5\lambda$ Abbe limit, all of them obey the fundamental resolution limit δ_{SI} given by Eq. (3).

5. DISCUSSION

It is worth noting that, in this paper, we combined both numerical analysis and experiments to verify the derived limits of a SI lens resolution [Eq. (3)]. First, we perform quite comprehensive numerical analysis for the two SI lens arrangements to justify the correctness of our theoretical considerations. Second, we accumulate and analyze quite a large amount of the experimental data on the spatial resolution of SI lenses with the different arrangements, materials, and spectral operation ranges, among them: our original SI lenses made of silicon [4,16,18,19], rutile [23], sapphire [20], and rutile micropowder-based composite [21]. We use these experimental data from the earlier-published papers to verify the derived limit in Fig. 5. Therefore, we claim that our SI lens resolution limit [Eq. (3)] and the data from Fig. 5 can be useful when analyzing or predicting the resolution of

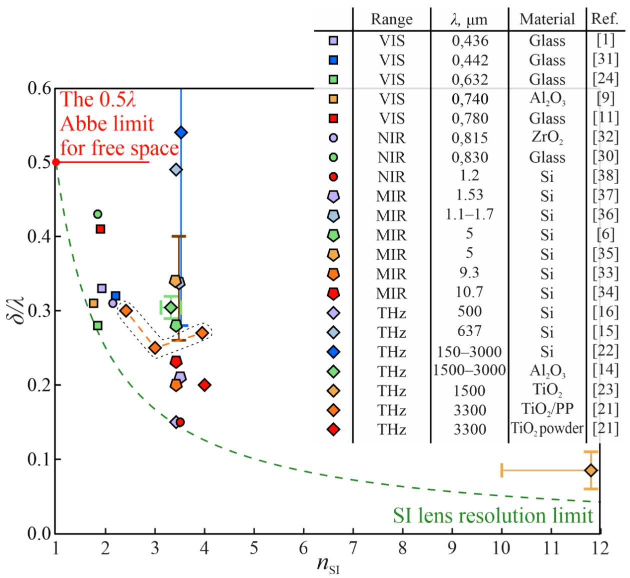

Fig. 5. Comparison of the resolution values normalized by the operation wavelength δ/λ reported for various VIS, NIR, MIR, and THz SI lenses. Also shown are the $\simeq 0.5\lambda$ Abbe limit and the fundamental resolution limit for SI lenses δ_{SI} given by Eq. (3). Horizontal bars reflect SI lens material birefringence, while the vertical ones stand for the SI lenses featuring the anisotropic beam spot, or designed for the broadband applications.

almost any novel SI lens, given the applied high-refractive-index material and operation wavelengths.

The resolution limit of SI optical systems established in this work will be useful for their further design and implementation, including the selection of appropriate high-refractive-index optical materials and lens geometries, aimed at meeting the demands of particular applications. Similar to the $\simeq 0.5$ and $\simeq 0.62$ Abbe diffraction limits for the 2D (cylindrical elements) and 3D optical systems, the derived resolution limit for a SI lens can be generalized from the 2D to 3D cases, where the same difference of several tens of percents is expected. However, when generalizing to 3D, one needs to take into account possible birefringence of the SI lens materials, beam polarization, focal spot anisotropy, and ultimately object-dependent performance of the SI optical systems [4,18,23]. Nevertheless, all these effects should lead to a reduction in the SI lens resolution and cannot help to overcome the fundamental resolution limit for a SI lens given by Eq. (3).

We pay attention to the numerical analysis of SI lenses, which focus the beam in an axial point and feature negligible fields of view. In such a case, the image is collected by a raster scan of an object by a beam caustic (focal spot), while a single-pixel detector is used. Despite the majority of SI lenses operating in such an axial-point regime, a wide-field SI lens also exists, with the finite field of view and matrix detectors [35,36,38–40]. For both the basic wide-aperture focusing element and the SI resolution enhancer, the wavefront aberrations increase (the resultant image quality drops) with increasing field angles. For example, the basic wide-aperture aspherical singlet [17] in our THz SI microscope from Ref. [16] features the diffraction-limited field of view as small as $2\omega = 5^{\circ}$, thus, limiting the total field of view of our SI system. Meanwhile, for the hemispherical and hyper-hemispherical SI lenses, the wavefront aberrations increase with increasing field of view, because the beam is not focused in the aplanatic point of a sphere at larger field angles. Moreover, the energy efficiency of a SI lens should be a function of the field of view, since at different field angles one should expect different Fresnel losses at the SI lens spherical surface, as well as the different TIR conditions at the SI lens–air/object interface [34,41]. Such a reduced image quality limits the reliability of the wide-field SI microscopes. Nevertheless, since the same propagating and evanescent waves contribute to the image formation at higher field angles, the derived SI lens resolution limit [Eq. (3)] should be relevant to the wide-field SI microscopes.

We focused on spatial resolution of a SI lens illuminated by a coherent plane wave with a homogeneous intensity distribution over the beam aperture. In fact, this agrees well with our experiments on THz SI microscopy with a backward-wave oscillator [16] or a continuous-wave IMPATT diode [23], as a continuous THz wave emitter. These two emitters and even the THz heat waves from humans and other objects appear to be coherent [42]. Thus, at the moment we have no option to study experimentally the SI microscopy operation together with the incoherent source or that with a finite coherence. Other research topics to be addressed are the annular-aperture SI lenses and speckle patterns (due to the finite coherence length and imaging of scattering media), as well as their impact on the SI microscope performance. However, these topics are out of the scope of this paper, and we postponed them to our future studies.

Finally, we notice that the inferred SI lens resolution limit [Eq. (3)] is eligible only for the large-scale ($\gg\lambda$) near-focal lenses (resolution enhancers), those exploiting the SI effect. Meanwhile, this limit is not relevant to the dielectric-microparticle-assisted microscopy [43,44], which often relies on the resonant (i.e., the Mie/Fabry–Perot resonances, whispering-gallery modes, etc.) electromagnetic-wave interactions with a mesoscale ($\sim\lambda$) dielectric sphere, cuboid [45,46], particle with a broken symmetry [47,48], or even the output end of an optical fiber [49]. In a resonant case, such interaction leads to the excitation of the so-called photonic jets–i.e., a sub-wavelength beam caustics with the lateral dimensions smaller than the Abbe limit [50]. One should not confuse these two modalities of super-resolution near-field microscopy. To date, the mesoscale dielectric-particle-assisted microscopy has been extensively studied in the visible and IR ranges, as well as transferred to the THz band [45,46]. Such systems operate in the near-field regime and can provide the resolution as high as $\sim 0.1\lambda$, which is a function of not only the refractive index, but also the dimensions and the shape of a mesoscale dielectric particle. As compared to the SI microscopy, the mesoscale dielectric-particle-assisted microscopy suffers from the problem of a small dielectric particle handling in front of the focal plane during imaging. Moreover, as pointed out in Ref. [51], a favorable combination of the SI and photonic jet phenomena is possible in high-refractive-index dielectric particles, which can further boost the spatial resolution, but which remains a topic for the separate full-blown study. One should notice that the inferred SI lens resolution limit [Eq. (3)] is not relevant for such a combined resolution enhancer.

6. CONCLUSIONS

In conclusion, the SI lens resolution limit was derived, examined numerically, and verified by the experimental literature data on the different SI lenses. This limit is defined by only the SI lens refractive index and the free-space wavelength. Our numerical simulations uncovered that both the hemispherical and hyper-hemispherical configurations of a SI lens obey this resolution limit. Our analysis of the earlier-reported SI systems, operating in the different spectral ranges and relying on the different high-refractive-index materials, demonstrated that they all obey the inferred limit. The results of this paper will be useful for the further design and applications of SI optics. Particularly, they will help to select the appropriate geometry and materials of a SI lens, considering the desired spatial resolution and energy efficiency of the resultant SI optical system.

Funding. Russian Science Foundation (22–79–10099); Natural Sciences and Engineering Research Council of Canada (Discovery grant).

Acknowledgment. The work of V.A.Z., K.I.Z., and N.V.C. on the analytical and numerical studies of the SI lens resolution was supported by the RSF Project. The work of M.S. on the literature analysis of the spatial resolution of the existing SI lenses was supported by the Discovery grant of the National Science and Engineering Research Council of Canada.

Disclosures. The authors declare no conflicts of interest.

Data availability. The data that support the findings of this study are available from the corresponding author upon reasonable request.

REFERENCES

1. S. Mansfield and G. Kino, "Solid immersion microscope," Appl. Phys. Lett. **57**, 2615–2616 (1990).
2. K. Serrels, E. Ramsay, P. Dalgarno, *et al.*, "Solid immersion lens applications for nanophotonic devices," J. Nanophoton. **2**, 021854 (2008).
3. N. Chernomyrdin, M. Skorobogatiy, D. Ponomarev, *et al.*, "Terahertz solid immersion microscopy: recent achievements and challenges," Appl. Phys. Lett. **120**, 110501 (2022).
4. V. Zhelnov, K. Zaytsev, A. Kucheryavenko, *et al.*, "Object-dependent spatial resolution of the reflection-mode terahertz solid immersion microscopy," Opt. Express **29**, 3553–3566 (2021).
5. W. Fan, B. Yan, Z. Wang, *et al.*, "Three-dimensional all-dielectric metamaterial solid immersion lens for subwavelength imaging at visible frequencies," Sci. Adv. **2**, e1600901 (2016).
6. S. Ippolito, S. Thorne, M. Eraslan, *et al.*, "High spatial resolution subsurface thermal emission microscopy," Appl. Phys. Lett. **84**, 4529–4531 (2004).
7. G. Lerman, A. Israel, and A. Lewis, "Applying solid immersion near-field optics to Raman analysis of strained silicon thin films," Appl. Phys. Lett. **89**, 223122 (2006).
8. M. Baba, T. Sasaki, M. Yoshita, *et al.*, "Aberrations and allowances for errors in a hemisphere solid immersion lens for submicron-resolution photoluminescence microscopy," J. Appl. Phys. **85**, 6923–6925 (1999).
9. Q. Wu, R. Grober, D. Gammon, *et al.*, "Imaging spectroscopy of two-dimensional excitons in a narrow GaAs/AlGaAs quantum well," Phys. Rev. Lett. **83**, 2652–2655 (1999).
10. V. Devaraj, J. Baek, Y. Jang, *et al.*, "Design for an efficient single photon source based on a single quantum dot embedded in a parabolic solid immersion lens," Opt. Express **24**, 8045–8053 (2016).
11. B. Terris, H. Mamin, D. Rugar, *et al.*, "Near-field optical data storage using a solid immersion lens," Appl. Phys. Lett. **65**, 388–390 (1994).
12. S. Ippolito, P. Song, D. Miles, *et al.*, "Angular spectrum tailoring in solid immersion microscopy for circuit analysis," Appl. Phys. Lett. **92**, 101109 (2008).
13. L. Wang, B. Bateman, L. Zanetti-Domingues, *et al.*, "Solid immersion microscopy images cells under cryogenic conditions with 12 nm resolution," Commun. Biol. **2**, 74 (2019).
14. A. Pimenov and A. Loidl, "Focusing of millimeter-wave radiation beyond the abbe barrier," Appl. Phys. Lett. **83**, 4122–4124 (2003).
15. B. Gompf, M. Gerull, T. Muller, *et al.*, "THz-micro-spectroscopy with backward-wave oscillators," Infrared Phys. Technol. **49**, 128–132 (2006).
16. N. Chernomyrdin, A. Kucheryavenko, G. Kolontaeva, *et al.*, "Reflection-mode continuous-wave 0.15λ -resolution terahertz solid immersion microscopy of soft biological tissues," Appl. Phys. Lett. **113**, 111102 (2018).
17. N. Chernomyrdin, M. Frolov, S. Lebedev, *et al.*, "Wide-aperture aspherical lens for high-resolution terahertz imaging," Rev. Sci. Instrum. **88**, 014703 (2017).
18. N. Chernomyrdin, M. Skorobogatiy, A. Gavdush, *et al.*, "Quantitative super-resolution solid immersion microscopy via refractive index profile reconstruction," Optica **8**, 1471–1480 (2021).
19. N. Chernomyrdin, D. Il'enkova, V. Zhelnov, *et al.*, "Quantitative polarization-sensitive super-resolution solid immersion microscopy reveals biological tissues' birefringence in the terahertz range," Sci. Rep. **13**, 16596 (2023).
20. A. Kucheryavenko, V. Zhelnov, D. Melikyants, *et al.*, "Super-resolution THz endoscope based on a hollow-core sapphire waveguide and a solid immersion lens," Opt. Express **31**, 13366–13373 (2023).
21. Q. Chapdelaine, K. Nallappan, Y. Cao, *et al.*, "Fabrication and characterization of a composite TiO_2-polypropylene high-refractive-index solid immersion lens for super-resolution THz imaging," Opt. Mater. Express **12**, 3015–3031 (2022).
22. D.-H. Choi, M. Kim, D. W. Park, *et al.*, "Broadband sub-wavelength terahertz subsurface imaging using a solid-immersion lens," Opt. Laser Technol. **174**, 110557 (2024).
23. V. Zhelnov, N. Chernomyrdin, G. Katyba, *et al.*, "Hemispherical rutile solid immersion lens for terahertz microscopy with superior 0.06-0.11λ resolution," Adv. Opt. Mater. **12**, 2300927 (2024).
24. K. Karrai, X. Lorenz, and L. Novotny, "Enhanced reflectivity contrast in confocal solid immersion lens microscopy," Appl. Phys. Lett. **77**, 3459–3461 (2000).
25. C. Liu and S.-H. Park, "Numerical analysis of an annular-aperture solid immersion lens," Opt. Lett. **29**, 1742–1744 (2004).
26. Y.-J. Yoon, W.-C. Kim, N.-C. Park, *et al.*, "Feasibility study of the application of radially polarized illumination to solid immersion lens-based near-field optics," Opt. Lett. **34**, 1961–1963 (2009).
27. K. Huang and Y. Li, "Realization of a subwavelength focused spot without a longitudinal field component in a solid immersion lens-based system," Opt. Lett. **36**, 3536–3538 (2011).
28. M. Born and E. Wolf, *Principles of Optics* (Cambridge University, 1999).
29. A. Maznev and O. Wright, "Upholding the diffraction limit in the focusing of light and sound," Wave Motion **68**, 182–189 (2017).
30. B. Terris, H. Mamin, and D. Rugar, "Near-field optical data storage," Appl. Phys. Lett. **68**, 141–143 (1996).
31. L. P. Ghislain, V. B. Elings, K. B. Crozier, *et al.*, "Near-field photolithography with a solid immersion lens," Appl. Phys. Lett. **74**, 501–503 (1999).
32. S. Bishop, J. Hadden, and R. Hekmati, "Enhanced light collection from a gallium nitride color center using a near index matched solid immersion lens," Appl. Phys. Lett. **120**, 114001 (2022).
33. D. Fletcher, K. Crozier, C. Quate, *et al.*, "Near-field infrared imaging with a microfabricated solid immersion lens," Appl. Phys. Lett. **77**, 2109–2111 (2000).
34. D. Fletcher, K. Crozier, C. Quate, *et al.*, "Refraction contrast imaging with a scanning microlens," Appl. Phys. Lett. **78**, 3589–3591 (2001).
35. D. Fletcher, "Thermal microscopy with a microfabricated solid immersion lens," Microscale Thermophys. Eng. **7**, 267–273 (2003).
36. G. Tessier, M. Bardoux, C. Bouue, *et al.*, "Back side thermal imaging of integrated circuits at high spatial resolution," Appl. Phys. Lett. **90**, 171112 (2007).
37. E. Ramsay, N. Pleynet, D. Xiao, *et al.*, "Two-photon optical-beam-induced current solid-immersion imaging of a silicon flip chip with a resolution of 325 nm," Opt. Lett. **30**, 26–28 (2005).

38. F. Köklü, J. Quesnel, A. Vamivakas, *et al.*, "Widefield subsurface microscopy of integrated circuits," Opt. Express **16**, 9501–9506 (2008).
39. S. M. Mansfield, W. R. Studenmund, G. S. Kino, *et al.*, "High-numerical-aperture lens system for optical storage," Opt. Lett. **18**, 305–307 (1993).
40. O. Breitenstein, F. Altmann, T. Riediger, *et al.*, "Lock-in thermal IR imaging using a solid immersion lens," Microelectron. Reliab. **46**, 1508–1513 (2006).
41. V. Chernomyrdin, N. V. Zhelnov, A. Kucheryavenko, *et al.*, "Numerical analysis and experimental study of terahertz solid immersion microscopy," Opt. Eng. **59**, 061605 (2019).
42. I. N. Dolganova, K. I. Zaytsev, A. A. Metelkina, *et al.*, "A hybrid continuous-wave terahertz imaging system," Rev. Sci. Instrum. **86**, 113704 (2015).
43. S. Perrin, Y. J. Donie, P. Montgomery, *et al.*, "Compensated microsphere-assisted interference microscopy," Phys. Rev. Appl. **13**, 014068 (2020).
44. S. Perrin, R. Pierron, P. Gerard, *et al.*, "Miniaturized microsphere-assisted microscopy," Appl. Phys. Lett. **122**, 161108 (2023).
45. H. N. Pham, S. Hisatake, O. Minin, *et al.*, "Enhancement of spatial resolution of terahertz imaging systems based on terajet generation by dielectric cube," APL Photon. **2**, 056106 (2017).
46. I. Dorofeev, V. Suslyaev, O. Minin, *et al.*, "Role of the tangential electric field component to the terahertz jet and hook formation by dielectric cube and sphere," Opt. Eng. **60**, 082004 (2020).
47. I. Minin, O. Minin, G. Katyba, *et al.*, "Experimental observation of a photonic hook," Appl. Phys. Lett. **114**, 031105 (2019).
48. S. Perrin, P. Montgomery, and S. Lecler, "Super-resolution imaging within reach," Opt. Eng. **58**, 050501 (2019).
49. D. Bouaziz, S. Perrin, T. Hajj, *et al.*, "Direct imaging of a photonic jet at shaped fiber tips," Opt. Lett. **46**, 5125 (2021).
50. B. S. Luk'yanchuk, R. Paniagua-Dominguez, I. V. Minin, *et al.*, "Refractive index less than two: photonic nanojets yesterday, today and tomorrow," Opt. Mater. Express **7**, 1820–1847 (2017).
51. L. Yue, B. Yan, J. Monks, *et al.*, "A millimetre-wave cuboid solid immersion lens with intensity-enhanced amplitude mask apodization," J. Infrared Millim. Terahertz Waves **39**, 546–552 (2018).